INFRARED SPECTROSCOPIC IMAGING OF THE BIOCHEMICAL MODIFICATIONS INDUCED IN THE CEREBELLUM OF THE NIEMANN–PICK TYPE C MOUSE

Linda H. Kidder,[†] Pina Colarusso,[†] Sarah A. Stewart,[†] Ira W. Levin,[†] Nathan M. Appel,[‡] David S. Lester,[‡] Peter G. Pentchev,[*] and E. Neil Lewis[†]

[†]Laboratory of Chemical Physics, National Institute of Diabetes, and Digestive and Kidney Diseases, The National Institutes of Health, Bethesda, Maryland 20892; [‡]Food and Drug Administration, Center for Drug Evaluation and Research, Division of Applied Pharmacology Research, Laurel, Maryland 20708; [*]National Institutes of Health, National Institute of Neurological Disorders and Stroke, Developmental and Metabolic Neurology Branch, Molecular and Cellular Pathology Section, Bethesda, Maryland 20892

ABSTRACT

We have applied Fourier transform infrared (IR) spectroscopic imaging to the investigation of the neuropathologic effects of a genetic lipid storage disease, Niemann–Pick type C (NPC). Tissue sections both from the cerebella of a strain of BALB/c mice that demonstrated morphology and pathology of the human disease and from control animals were used. These samples were analyzed by standard histopathological procedures as well as this new IR imaging approach. The IR absorbance images exhibit contrast based on biochemical variations and allow for the identification of the cellular layers within the tissue samples. Furthermore, these images provide a qualitative description of the localized biochemical differences existing between the diseased and control tissue in the absence of histological staining. Statistical analyses of the IR spectra extracted from individual cell layers of the imaging data sets provide concise quantitative descriptions of these biochemical changes. The results indicate that lipid is depleted specifically in the white matter of the NPC mouse in comparison to the control samples. Minor differences were noted for the granular layers, but no significant differences were observed in the molecular layers of the cerebellar tissue. These changes are consistent with significant demyelination within the cerebellum of the NPC mouse. © 1999 Society of Photo-Optical Instrumentation Engineers. [S1083-3668(99)00401-3]

Keywords infrared spectroscopic imaging; FTIR spectroscopy; Niemann–Pick type C; neuropathology, cerebellum.

1 INTRODUCTION

Infrared (IR) spectroscopic imaging is an analytical technique that simultaneously visualizes the morphology and molecular composition of systems down to the micron level. The hallmark of this approach is the rapid, parallel acquisition of IR spectra for thousands to tens-of-thousands of contiguous points on a sample. Since a spectrum is recorded at each spatial location, the resulting data may be represented as a three-dimensional image cube. As depicted in Figure 1, the image cube contains both spatially resolved spectra and wavelength dependent images. Since IR spectroscopic imaging encodes spatial variations in chemical composition, the methodology is ideal for probing heterogeneous chemical or biological systems.

Fourier transform infrared (FTIR) spectroscopic imaging is typically implemented with a step-scan interferometer, in which the single element detector used in conventional FTIR spectroscopy is replaced with a two-dimensional infrared focal-plane array (FPA). These IR FPAs, which were initially produced for military utilization, are the key enabling technology for spectroscopic imaging at infrared wavelengths. In addition to their having been adopted by the remote sensing and astronomical communities,[1,2] the recent increased availability and reduced cost of FPAs has led to the growth of IR spectroscopic imaging microscopy as an analytical tool in a variety of industrial and research settings.[3–5] In particular, the combination of an in-

Address all correspondence to E. Neil Lewis, 9000 Rockville Pike, Building 5, Room B1-38, Bethesda, MD 20892-0510; Phone: (310) 496-6847; Fax: (310) 496-0825; E-mail: neil@spy.niddk.nih.gov
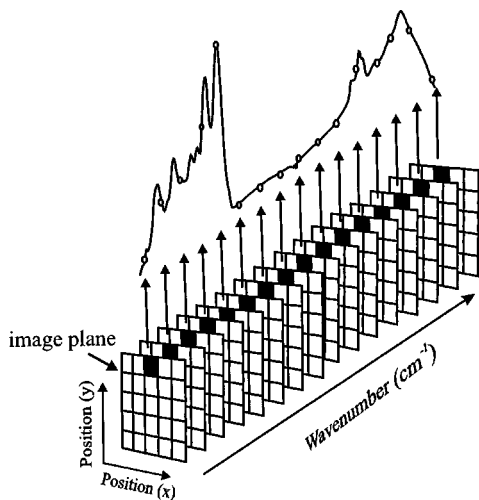
Fig. 1 FTIR spectroscopic imaging data represented as an ''image cube,'' having one spectral and two spatial dimensions.

terferometer and FPA represents an effective and flexible apparatus for spectroscopic imaging at mid-IR wavelengths, the standard spectral interval for chemical analysis. Even the most modest of interferometers is capable of recording spectra with variable resolutions, including 1 cm^{-1} or better. Imaging data recorded using these interferometers demonstrate the same attributes, which are equivalent, or superior, to the current state of the art obtainable with fixed bandpass tunable filters typically used in other optical spectroscopic imaging approaches.[6,7] Additionally, close to diffraction limited image quality is obtainable.[8] A further significant advantage of this approach is the immense flexibility in terms of sampling field of view: objects on both astronomical or cellular scales can be imaged.[9] As a result, either broad trends or the finer details of both morphology and chemistry can be elucidated using this technique.

One emerging application of FTIR spectroscopic imaging is the characterization of medical and biological systems. This technique builds on a wealth of single-point and mapping measurements, which have demonstrated the utility of conventional IR spectroscopy in analyzing biochemical heterogeneity.[10–14] Indeed, more recent studies have concluded that FTIR spectroscopic imaging may prove to be useful in diagnostic pathology, since it incorporates the imaging capabilities required for histological procedures with the chemical discrimination of IR spectroscopy.[15] Thus far, this FTIR imaging approach has been employed in the analyses of silicone oil leakage from an implanted prosthetic in breast tissue and studies of the neurotoxicity of an antineoplastic drug, cytarabine.[5,15] Preliminary FTIR spectroscopic images of colon carcinoma have also been obtained.[16]

In this report, we have undertaken an FTIR imaging study of the lethal childhood neurodegenerative genetic disease, Niemann–Pick type C (NPC).

NPC is an autosomal recessive neurovisceral lipid storage disease that, amongst other effects, obstructs the intracellular trafficking of exogenous low density lipoprotein cholesterol. NPC diseased children usually present with progressive seizures, dystonia, and dementia in late childhood, and die within the second decade of life. The pathological manifestations of the disease are diverse, and many experimental protocols have been used in its study. Symptoms of NPC are largely neurological in nature; thus, many studies have focused on the neuropathology of the disease.[17–22] Within the brain, NPC often produces a degeneration of the cerebellum due to the rapid loss of the Purkinje cells. In the later stages of the disease, cerebellar atrophy has also been noted.[17] Studies that have focused on the biochemical rather than the clinical or morphological manifestations of NPC have attempted to characterize gross changes induced in the relative amounts of lipids and cholesterol in organs such as the liver, spleen, and brain.[17–22] Many of these studies have characterized cell-free extracts that investigate homogenized specimens, and therefore provide little spatial information on the biochemical changes occurring within specific cell layers.[19–22] Consequently, the existing literature reports varying results. In particular, both increases in apolipoprotein D (associated with myelin) and demyelination in the white matter of the cerebellum have been reported as neuropathological manifestations of NPC in mouse models.[20,21]

Because FTIR spectroscopic imaging has the ability to visualize and quantify the differences in the biochemical composition of discrete cellular layers within intact tissue specimens, it should be particularly useful for visualizing the changes induced in the composition of tissue resulting from a storage disease, such as NPC. To this end, we have applied FTIR spectroscopic imaging to study and to compare sagittal sections derived from the cerebella of both control and NPC mice.

2 EXPERIMENT

2.1 MOUSE MODEL AND ANIMAL PREPARATION

Two BALB/c mice (50 day old) prominently displaying an advanced degenerative state of NPC disease and two control animals from the parental strain from which the BALB/c mutant was derived were obtained. The clinical descriptions, preparation, and identification of the BALB/c NPC mice has been reported previously.[23,24] Four animals were sacrificed; their brains were rapidly removed and immediately frozen by covering with powdered dry ice. Samples were kept at $-80°C$ until the time of sectioning. Frozen sagittal sections were cut (10 μm) on a cryostat (Hacker, Fairfield, NJ) at a temperature of $-21°C$. The slices were mounted onto calcium fluoride (CaF$_2$) disks (Wilmad Glass,
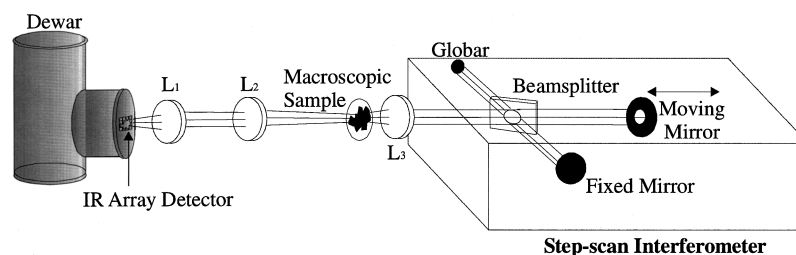
Fig. 2 Step-scan infrared imaging system, incorporating a commercial FTIR step-scan interferometer with a liquid-nitrogen cooled InSb FPA detector containing 128×128 pixels. The infrared emission is focused onto the sample and then transmitted to the FPA through a series of IR transmissive lenses (L_1, L_2, and L_3). The focal lengths of L_1, L_2, and L_3 are 150, 50, and 150 mm, respectively.

Buena, NJ) and were stored with dessicant at room temperature. Infrared spectroscopic imaging data sets were recorded from four tissue sections, two from normal animals, and two from diseased mice.

2.2 HISTOPATHOLOGY

Contiguous 10 μm tissue sections were prepared for the FTIR specimens. The mounted sections were defatted with xylene, rehydrated through a series of graded alcohols, stained for 15 min in cresyl violet for purposes of comparison with the IR spectroscopic images.[25] Cresyl violet is a Nissl stain that preferentially binds to neuronal cytoplasmic material.[26,27]

2.3 MACROSCOPIC INFRARED SPECTROSCOPIC IMAGING

The experiments were conducted with an IR spectroscopic imaging system consisting of a step-scan interferometer, macroscopic image formation optics, and an IR FPA developed in this laboratory.[8,28] In this arrangement, as shown in Figure 2, the emission from a ceramic globar is modulated by a step-scan interferometer (Bio-Rad FTS 6000, Cambridge, MA) and focused onto the sample by a series of CaF_2 lenses. The transmitted radiation is then imaged onto a liquid nitrogen cooled indium antimonide (InSb) FPA (Lockheed/Santa Barbara Focal Plane, Goleta, CA) with a magnification of approximately 1.2. The InSb FPA detector, consisting of 128 ×128 50 μm pixels, has a spectral range of 1–5.5 μm (10 000–1820 cm^{-1}). The step-scan/FPA system is described more fully in previous publications.[8,29] In this study, data were collected at 16 cm^{-1} spectral resolution with an interferometer step rate of 0.1 Hz. At each interferometer step, a total of 320 frames were collected at a rate of 65.6 Hz, with a 2.14 ms integration time per frame. The resulting data consisted of 256 image planes and a total of 16 384 interferograms, corresponding to the 128 ×128 image pixels. The individual interferograms were apodized and Fourier transformed to create a series of frequency resolved images and spectra. These single beam spectra were divided by an averaged air background spectrum to yield transmittance spectra and images, which are subsequently converted to absorbance images and spectra. A simple two-point baseline correction was then applied over the spectral range (~3600–2600 cm^{-1}).

3 RESULTS AND DISCUSSION

Figure 3 presents stained histopathological and FTIR spectroscopic images of control and NPC tissue sections. The samples consisted of 10-μm-thick saggital sections of intact mouse brain. The stained sections highlight the cellular organization within the cerebella, corresponding to the white matter, the granular layer, and the molecular layer. Analogous to the histopathological images, the FTIR spectroscopic images delineate the cellular layers. In these images, however, the contrast is derived without the application of external stains or markers. The FTIR spectroscopic images were obtained from the ratioed intensities of two characteristic mid-IR absorptions, the CH_2 asymmetric stretching modes at 2927 cm^{-1}, and the protein amide A mode centered at 3290 cm^{-1}. The methylene absorption at 2927 cm^{-1} has contributions from primarily the lipid acyl chain modes, with some contribution from the methyl modes of the protein side chains. The ratioed images depict the relative strengths of the lipid and protein bands: the brighter the pixel, the higher the relative lipid content. For both the control and NPC sections, the spectroscopic images reveal that white matter contains the highest relative amount of lipid, followed by the molecular and granular layers. This finding is consistent with the biochemical composition of brain tissue. Additionally, it should be noted that the relative brightness of the white matter is reduced in the diseased section compared to the control. This qualitative observation is consistent with a reduction of lipid in the white matter of the diseased animal. However, the power of FTIR spectroscopic imaging can be more readily appreciated by examining the quantitative chemical information contained within the individual infrared spectra that are available for each image pixel: each data set contains 128×128=16 384 spectra over the imaged sample area. Representative FTIR spectra were extracted from each data cube, and grouped according to cellular layer. As the physical delineation of these layers cannot be
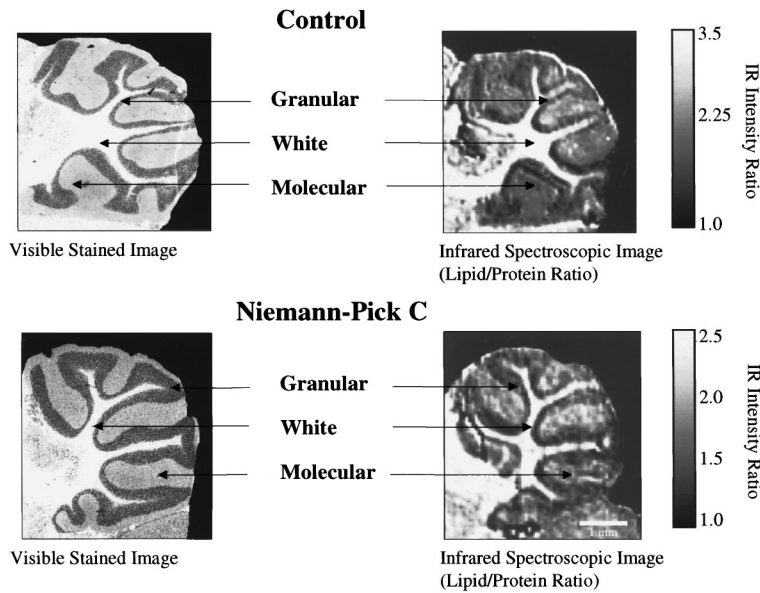
Fig. 3 Infrared spectroscopic and histopathological images of 10-μm-thick cerebellar sections from control and NPC diseased animals. The histopathological sections (left) are prepared with Nissl stain. FTIR spectroscopic images from unstained sections (right) depict the distribution of lipid and protein within the sample. These images were obtained from the ratioed intensities of two characteristic mid-IR absorptions, the CH_2 asymmetric stretch at 2927 cm^{-1} and protein amide A mode centered at 3290 cm^{-1}.

described by a simple geometric algorithm, it is difficult to automatically classify all of the spectra contained within the data set as to anatomical layer. However, by overlaying an infrared bright field image from the data set in which the morphology can be distinguished, pixels can be visually classified as to cellular layer and the corresponding spectra selected. Although this type of sampling does not utilize each spectrum contained within the data set, it does enable the collection of many representative spectra from each cellular layer, comprising a statistical sampling. Care was taken to select pixels that were well characterized (i.e., not to select pixels on cell layer borders), and to collect enough pixels to provide a representative sampling: up to 567 pixels per cell layer were selected for each tissue sec-

tion. The number of spectra collected for each sample and cellular layer varies because of differences in their physical dimensions. Table 1 lists the number of spectra that were sampled from each layer and the statistics associated with the relative lipid content of each.

Figure 4 illustrates spectra for one of the control tissue samples; each trace is the mean of the representative infrared spectra for the white matter, granular layer, and molecular layer, respectively. Two prominent spectral features arise: the protein amide A vibration is centered at approximately 3290 cm^{-1} and the lipid and protein CH stretching modes are centered at approximately 2927 cm^{-1}. The band intensities for these spectra have been

Table 1 Statistical summary of the relative lipid to protein ratios for the control and NPC sections.

| Cellular layer | Control | | | | | | NPC model | | | | | |
| | Control 1 | | | Control 2 | | | Diseased 1 | | | Diseased 2 | | |
	Number of spectra selected[+]	Mean lipid to protein ratio[♦]	Variance	Number of spectra selected[+]	Mean lipid to protein ratio[♦]	Variance	Number of spectra selected[+]	Mean lipid to protein ratio[♦]	Variance	Number of spectra selected[+]	Mean lipid to protein ratio[♦]	Variance
White	159	2.51	0.43	263	2.24	0.27	178	1.71	0.19	143	1.60	0.17
Granular	483	1.26	0.07	567	1.06	0.04	360	1.05	0.04	427	1.01	0.03
Molecular	322	1.28	0.01	360	1.15	0.01	270	1.15	0.01	183	1.13	0.01

[+] Spectra were selected at random points within the cellular layers.

[♦] Calculated using absorbance values of the peak maxima of the asymmetric CH_2 stretching mode (2927 cm^{-1}) and the protein amide A mode (3290 cm^{-1}).
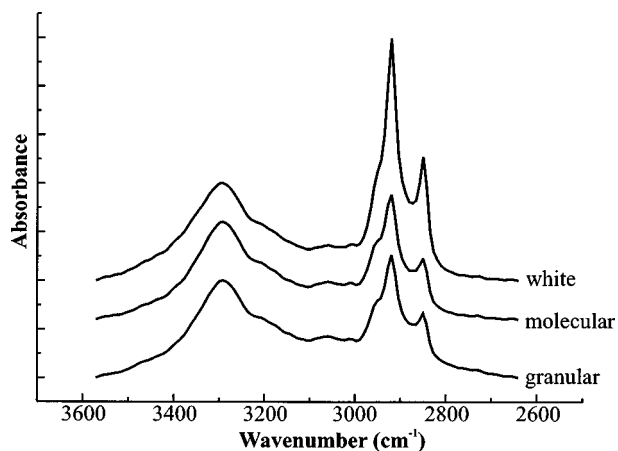
Fig. 4 Spectra from a control tissue sample normalized to the protein amide A mode. Each trace is the mean representative infrared spectrum for the individual cellular layers (offset for clarity).

normalized to the amide A band, which implies that variations in the intensities of the CH_2 stretching modes can be attributed primarily to differences in the lipid content. Just as seen in the infrared images shown in Figure 3, the spectra reveal that the lipid content varies across cell layers, with the white matter containing more lipid than either

the granular or molecular layers. Although these variations in the lipid concentration across cellular layers of the brain are known, the origin of the differences between the NPC and control cerebella is unexplored. Infrared spectroscopic imaging, however, provides the opportunity to derive quantitative and statistically relevant data to address this problem.

As previously stated, the images in Figure 3 provide an understanding of distribution by cellular layer of lipid and protein. However, this representation provides no means for statistically assessing quantifiable differences within or between samples. The infrared spectra contained within the data sets though can be utilized to quantitatively summarize the data. Figure 5 presents three panels that plot the absorbance value at 3290 cm^{-1} (protein) versus the absorbance value at 2927 cm^{-1} (lipid) for each of the pixels used to derive the values presented in Table 1. The results obtained for both NPC and normal sections are pooled and displayed on the same plot. The dark circles for all three panels are derived from spectra from the NPC animals, while the open circles are spectra derived from the controls. From examination of all three panels, it can be discerned that a visible difference exists in the clustering of the data for the white matter in the controls versus
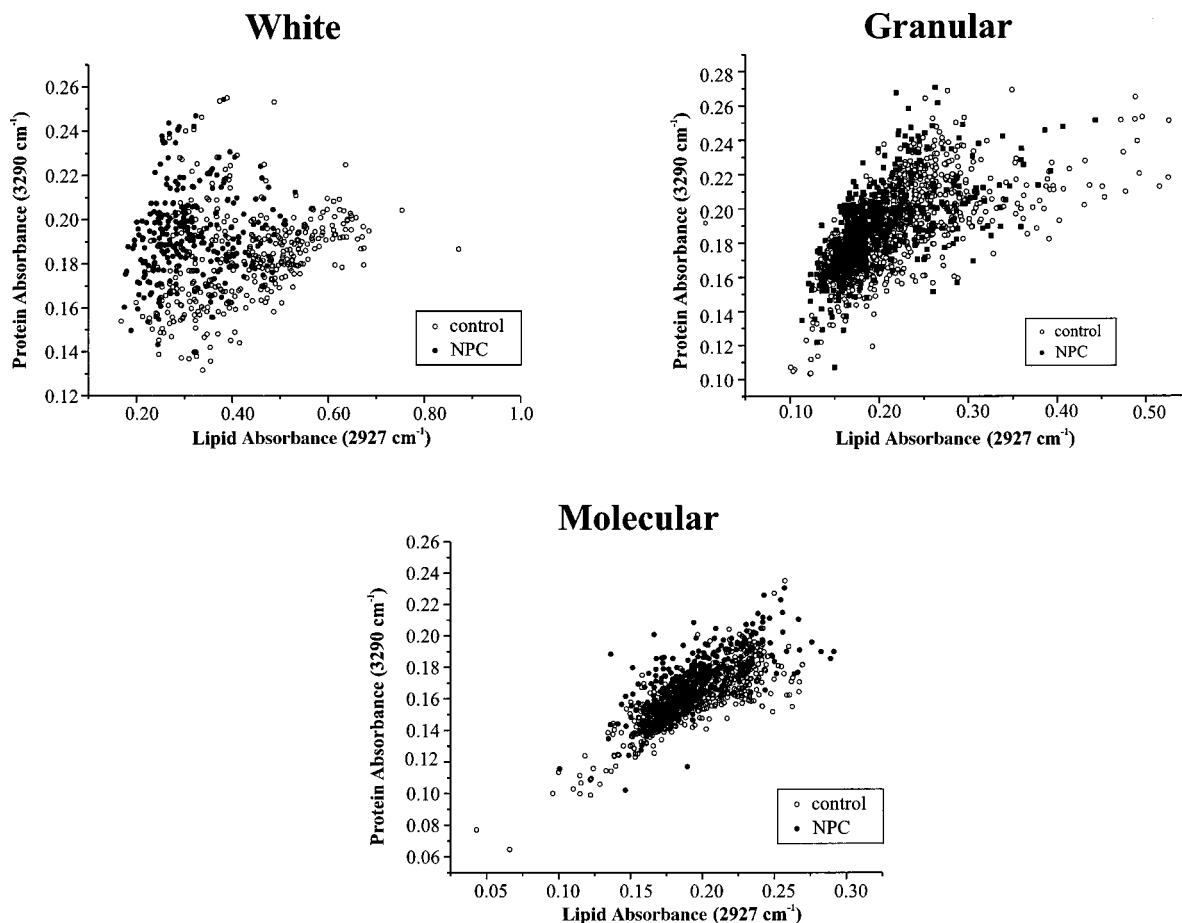

Fig. 5 Scatter plots of the protein and lipid absorbances from the representative spectra for each cellular layer.

the NPC mouse. The NPC data lie closer to the protein axis, indicating less lipid than the corresponding control spectra. Modest differences are also noted for the granular layer, with no visible differences discerned for the molecular layer.

While Table 1 indicates that the highest mean lipid to protein ratios is measured for the control sections, a statistical comparison of the differences between samples can be made using the technique of analysis of variance (ANOVA). Employing the pooled data from Figure 5, we calculate that there is a statistically significant decrease in the amount of lipid in all three cellular layers at the 95% confidence level. However, it is clear from the table that Control 1 has a significantly higher mean lipid to protein ratio than does Control 2. When the control and diseased section data are pooled, therefore, Control 1 weights the data so that differences between the normal and diseased sections are noted in all three cell layers. Utilization of the same statistical approach to compare the two control samples indicates that their lipid levels also statistically differ in all three cell layers. When an ANOVA analysis is performed comparing Control 2 and Diseased 1, which exhibit the most similarities between control and diseased sections (see Table 1), a statistically significant difference is only noted for the white matter, while the differences between granular and molecular layers are not considered significantly at the 95% confidence level. These analyses suggest that there are significant decreases in the lipid content of the diseased sections relative to the controls. It is less clear whether these differences are isolated within the white matter or are seen in the other cellular layers. While this infrared imaging approach can provide excellent intrasample statistics related to biochemical composition, an intersample statistical comparison would be more robust with the analysis of a larger number of sections.

4 Conclusions

We have applied FTIR spectroscopic imaging to the investigation of NPC in a mutant mouse strain. The technique provides a mechanism for the visualization of the distribution of intrinsic biochemical components such as lipids and proteins, while the individual spectra provide a tool for the quantitative and statistical determination of these differences. In addition, we have also shown how this technique can nondestructively probe the individual cell layers and extract useful biochemical parameters pertaining to each cell layer. In conclusion, we foresee FTIR spectroscopic imaging as a technique that will augment existing histopathology and, unlike other imaging methodologies, will simultaneously provide quantitative chemical data that describes the biochemical heterogeneities within the sample.

References

1. J. F. Arens, G. M. Lamb, M. C. Peck, H. Moseley, W. F. Hoffman, R. Tresch-Fienberg, and C. G. Fazio, ''High spatial resolution observations of NGC 7027 with a 10-μm array camera,'' *Astrophys. J.* **279**, 685–691 (1984).
2. A. F. H. Goetz, G. Vane, J. E. Solomon, and B. N. Rock, ''Imaging spectrometry for earth remote sensing,'' *Science* **228**, 1147–1153 (1985).
3. C. Marcott and R. C. Reeder, ''FT-IR spectroscopic imaging using an MCT focal-plane array detector,'' *AIP Conf. Proc.* **430**, 377–378 (1997).
4. R. Bhargava, S.-Q. Wang, and J. L. Koenig, ''FT-IR imaging of the interface in multicomponent systems using optical effects induced by differences in refractive index,'' *Appl. Spectrosc.* **52**, 323–338 (1998).
5. L. H. Kidder, V. F. Kalasinsky, J. L. Luke, I. W. Levin, and E. N. Lewis, ''Visualization of silicone gel in human breast tissue using new infrared imaging spectroscopy,'' *Nat. Med.* (*N.Y.*) **3**, 235–237 (1997).
6. S. R. Goldstein, L. H. Kidder, T. M. Herne, I. W. Levin, and E. N. Lewis, ''The design and implementation of a high fidelity Raman imaging microscope,'' *J. Microsc.* **184**, 34–45 (1996).
7. H. R. Morris, C. C. Hoyt, P. Miller, and P. J. Treado, ''Liquid crystal tunable filter Raman chemical imaging,'' *Appl. Spectrosc.* **50**, 805–811 (1996).
8. E. N. Lewis, P. J. Treado, R. C. Reeder, G. M. Story, A. E. Dowrey, C. Marcott, and I. W. Levin, ''Fourier transform spectroscopic imaging using an infrared focal-plane array detector,'' *Anal. Chem.* **67**, 3377–3381 (1995).
9. P. Colarusso, L. H. Kidder, I. W. Levin, J. C. Fraser, and E. N. Lewis, ''Infrared spectroscopic imaging: From planetary to cellular systems,'' *Appl. Spectrosc.* **52**, 106A–120A (1998).
10. D. M. Haaland, H. D. T. Jones, and E. V. Thomas, ''Multivariate classification of the infrared spectra of cell and tissue samples,'' *Appl. Spectrosc.* **51**, 340–345 (1997).
11. S. M. LeVine and D. L. Wetzel, ''*In situ* chemical analyses from frozen tissue sections by Fourier transform infrared microspectroscopy: Examination of white matter exposed to extravasated blood in the rat brain,'' *Am. J. Pathol.* **145**, 1041–1047 (1994).
12. E. P. Paschalis, O. Jacenko, B. Olsen, R. Mendelsohn, and A. L. Boskey, ''Fourier transform infrared microspectroscopic analysis identifies alterations in mineral properties in bones from mice transgenic for type X collagen,'' *Bone* (*N.Y.*) **19**, 151–156 (1996).
13. C. P. Schultz and H. H. Mantsch, ''Biochemical imaging and 2D classification of keratin pearl structures in oral squamous cell carcinoma,'' *Cell. Mol. Biol.* **44**, 203–210 (1998).
14. L. Chiriboga, X. P. Vigorita, D. Zarou, D. Zakim, and M. Diem, ''Infrared spectroscopy of human tissue. II. A comparative study of spectra of biopsies of cervical squamous epithelium and of exfoliated cervical cells,'' *Biospectroscopy* **4**, 55–59 (1998).
15. D. S. Lester, L. H. Kidder, I. W. Levin, and E. N. Lewis, ''Infrared microspectroscopic imaging of the cerebellum of normal and cytarabine treated rats,'' *Cell. Mol. Biol.* **44**, 29–38 (1998).
16. P. Lasch and D. Naumann, ''FT-IR microspectroscopic imaging of human carcinoma thin sections based on pattern recognition techniques,'' *Cell. Mol. Biol.* **44**, 189–202 (1998).
17. Y. Higashi, S. Murayama, P. G. Pentchev, and K. Suzuki, ''Cerebellar degeneration in the Niemann–Pick type C mouse,'' *Acta Neuropathol.* **85**, 175–184 (1993).
18. Y. J. Tanaka, H. Nakamura, and S. Miyawaki, ''Cerebellar involvement in murine sphingomyelinosis: A new model of Niemann–Pick disease,'' *J. Neuropathol. Exp. Neurol.* **47**, 291–300 (1988).

19. S. Schedin, P. G. Pentchev, U. Brunk, and G. Dallner, ''Changes in the levels of dolichol and dolichol phosphate in a murine model of Niemann–Pick's type C disease,'' *J. Neurochem.* **65**, 670–676 (1995).

20. S. Suresh, Z. Yan, R. C. Patel, Y. C. Patel, and S. C. Patel, ''Cellular cholesterol storage in the Niemann–Pick disease type C mouse is associated with the increased expression and defective processing of apoliproprotein D,'' *J. Neurochem.* **70**, 242–251 (1998).

21. H. Weintraub, A. Abramovici, U. Sandbank, P. G. Pentchev, R. O. Brady, M. Sekine, A. Suzuki, and B. Sela, ''Neurological mutation characterized by the dysmyelination in NCTR-Balb/C mouse with lysosomal lipid storage disease,'' *J. Neurochem.* **45**, 665–672 (1985).

22. M. Elleder, M. A. Jirasek, F. Smid, J. Ledvinova, and G. T. N. Besley, ''Niemann disease type C. Study on the nature of the cerebral storage process,'' *Acta Neuropathol.* **66**, 325–336 (1985).

23. S. K. Loftus, J. A. Morris, E. D. Carstea, J. Z. Gu, C. Cummings, A. Brown, J. Ellison, K. Ohno, M. A. Rosenfeld, D. A. Tagle, P. G. Pentchev, and W. J. Pavan, ''Murine model of Niemann–Pick C disease: Mutation in a cholesterol homeostasis gene,'' *Science* **277**, 232–235 (1997).

24. P. G. Pentchev, M. T. Vanier, K. Suzuki, and M. C. Patterson, ''Niemann–Pick disease, type C: A cellular cholesterol lipidosis,'' in *The Metabolic and Molecular Basis of Inherited Disease*, C. R. Scriver, A. L. Beaudet, W. S. Sly, and D. Valle, Eds., Chap. 85, pp. 2625–2640, McGraw–Hill, New York (1995).

25. G. Paxinos and C. Watson, *The Rat Brain in Stereotaxic Coordinates*, 2nd ed., Academic, San Diego (1986).

26. P. Hecht, *Dye Powders for Biological Staining No. 103*, Rowley Biochemical Institute, Rowley (1983).

27. R. D. Lillie, *H. J. Conn's Biological Stains*, 9th ed., Williams and Wilkins, Baltimore (1977).

28. E. N. Lewis, I. W. Levin, and P. J. Treado, ''Spectroscopic imaging devices employing imaging quality spectral filters,'' U.S. Patent No. 5,377,003 (1994).

29. L. H. Kidder, V. D. Kleiman, E. J. Heilweil, I. W. Levin, and E. N. Lewis, ''Mercury cadmium telluride (MCT) focal-plane array detection for mid-infrared Fourier-transform spectroscopic imaging,'' *Opt. Lett.* **22**, 742–744 (1997).